# Soft Matter

Accepted Manuscript


This is an *Accepted Manuscript*, which has been through the Royal Society of Chemistry peer review process and has been accepted for publication.

*Accepted Manuscripts* are published online shortly after acceptance, before technical editing, formatting and proof reading. Using this free service, authors can make their results available to the community, in citable form, before we publish the edited article. We will replace this *Accepted Manuscript* with the edited and formatted *Advance Article* as soon as it is available.

You can find more information about *Accepted Manuscripts* in the Information for Authors.

Please note that technical editing may introduce minor changes to the text and/or graphics, which may alter content. The journal's standard Terms & Conditions and the Ethical guidelines still apply. In no event shall the Royal Society of Chemistry be held responsible for any errors or omissions in this *Accepted Manuscript* or any consequences arising from the use of any information it contains.

ROYAL SOCIETY OF CHEMISTRY

www.rsc.org/softmatter

# Flow-induced 2D protein crystallization: Characterization of the coupled interfacial and bulk flows

**James E. Young,[a] David Posada,[a] Juan M. Lopez[b] and Amir H. Hirsa*[a]**

Two-dimensional crystallization of the protein streptavidin, crystallizing below a biotinylated lipid film spread on a quiescent air-water interface is a well studied phenomenon. More recently, 2D crystallization induced by a shearing interfacial flow has been observed at film surface pressures significantly lower than those required in a quiescent system. Here, we quantify the interfacial and bulk flow associated with 2D protein crystallization through numerical modeling of the flow along with a Newtonian surface model. Experiments were conducted over a wide range of conditions resulting in a state diagram delineating the flow strength required to induce crystals for various surface pressures. Through measurements of the velocity profile at the air-water interface, we found that even in the cases where crystals are formed, the macroscopic flow at the interface is well described by the Newtonian model. However, the results show that even in the absence of any protein in the system, the viscous response of the biotinylated lipid film is complicated and strongly dependent on the strength of the flow. This observation suggests that the insoluble lipid film plays a key role in flow-induced 2D protein crystallization.

## 1 Introduction

Many advances in our understanding of biological systems at the molecular level have been made possible through detailed knowledge of the structure of proteins and nucleic acids. The ability to describe and utilize protein structure and to define interactions with ligands has made possible the rational design of new drugs and pharmacological agents.[1–3] The primary technique that yields a detailed description of protein structure is X-ray crystallography. However, before this powerful technique can be utilized, the protein must first be crystallized. Crystallographers acknowledge that growing crystals is often the major bottleneck in structure determination.[4] Here, we show that fluid dynamics holds the potential to accelerate the protein crystallization process, thus offering a new avenue for progress.

Two-dimensional protein crystallization has advantages over growing crystals in 3D. For example, 2D systems are not affected by gravity, an issue that plagues 3D crystallographers. Attempts have been made to grow crystals in near-zero gravity environments as a means of overcoming gravity-related problems.[5] Another advantage of 2D crystallization is that the protein is concentrated at the interface, requiring much smaller quantities of protein in solution, typically three orders of magnitude less. In practice, this may be crucial for membrane proteins due to the difficulty in obtaining them in large quantities. Even for water-soluble proteins, which are of current interest, the relatively high cost of the protein strongly favors 2D crystallization.

[a] *Department of Mechanical, Aerospace and Nuclear Engineering, Rensselaer Polytechnic Institute, Troy, NY 12180-3590, USA*
[b] *School of Mathematical and Statistical Sciences, Arizona State Univ., Tempe AZ, 85287, USA*
* *E-mail: hirsaa@rpi.edu*

Two-dimensional protein crystallization commonly entails the injection of protein into a quiescent aqueous pool below a previously spread ligand-bearing insoluble lipid film. The protein is able to specifically bind to the lipid film and rearrange itself to form highly-ordered 2D protein arrays, i.e. crystals. The protein crystallized most extensively is streptavidin which has a high binding affinity to biotin (vitamin $B_7$).[6–15] Interest in the interaction between streptavidin and biotin goes well beyond 2D crystallization since the streptavidin-biotin system is a workhorse in biotechnology.[16–19] The dissolved streptavidin in the bulk liquid anchors to the ligands in the biotinylated lipid film. Due to a high concentration of protein at the interface and fluidity of the film, the protein self-assembles into the crystal form.

Almost all studies of 2D protein crystallization have been carried out under quiescent conditions, i.e. without fluid flow. The use of fluid dynamics has been suggested or implemented in a few cases. In Vénien-Bryan *et al.*[20] and Lenne *et al.*[21] shear stress was applied to the lipid film by a rotating float disk in order to use ellipsometry to monitor the adsorption of proteins to the lipid film. In Drazek *et al.*[22] the use of a deep-channel flow geometry was suggested in order to enhance protein crystallization by controlling the spatial distribution of the protein at the air-water interface and to introduce advection to overcome the diffusion limit in the bulk, but no results of the effects of flow on crystals were shown. On the other hand, the literature on the hydrodynamics of proteins at the air-water interface in the absence of crystallization is extensive, using both macro-rheology[23,24] and micro-rheology.[25]

Azadani *et al.*[26] first showed that interfacial shear can produce 2D protein crystals at significantly smaller supersaturation. They reported a case where 2D protein crystals were obtained in the presence of bulk flow at about a tenth of the surface pressure needed for crystallization in a quiescent system.

Note that the surface pressure, Π, of an interface with a film is defined as the reduction in surface tension below its value for a clean interface. Furthermore, and perhaps more importantly from a practical perspective, flow sped up the crystallization process by at least a factor of three. The experimentally observed speed up of 2D crystallization due to flow is contrary to the effect of flow on crystallization of soft colloidal particles where molecular dynamic simulations have predicted a slowing of the crystallization process.[27]

Various possibilities for why flow induces 2D crystals include advection of protein to the surface by the bulk flow,[22] compression of the ligand-bearing lipid film by the flow,[26] and lowering of thermodynamic barriers for crystallization by interfacial shear. The buoyancy of protein solution injected into the bulk, due to its lower salt concentration, makes it unlikely that advection to the interface is the primary mechanism. Specifically, the difference between the index of refraction of the protein solution and the bulk fluid, due to their different salt concentrations, makes the plume of injected solution visible through the glass sidewall of our flow device. Upon injection into the bulk fluid, the protein visibly rises to the interface. The protein solution then slowly mixes with the surrounding solution to create a buffer with a homogeneous density, and is no longer distinctly visible. Furthermore, in other experiments where an oscillatory-driven bulk flow advects protein to and from the surface, but does not significantly shear it, have not induced crystallization.[28]

Compression of the monolayer was investigated by Azadani *et al.*[26] and was ruled out as a likely mechanism. This then raises the question of whether the one data point observed by Azadani *et al.*[26] was a fluke of nature. The present systematic experimental study shows that it was not.

Here we show that shear in the vicinity of the interface is the primary mechanism for flow-induced 2D protein crystallization. First, we determined the minimum flow strength needed to induce protein crystallization for a given surface pressure. We provide a detailed analysis of the coupled bulk and interfacial flow for a wide range of flow conditions. Then, in order to isolate flow-induced changes in the lipid film, we examined how flow affects the response of the film to shear in the absence of protein. The binary lipid film, which is essential in the crystallization process, was found to have a flow-dependent interfacial viscous response. The interplay between interfacial shear and phospholipid films is of intrinsic interest in and of itself since it provides insight into the complex behaviors occurring in lipid membranes that are vital to the survival of living cells.[29–32] The lipid film commonly used for 2D crystallization of streptavidin, as well as in this study, consists of two different phospholipids, one bearing the target ligand (biotin-X-DHPE) and the other a diluting lipid (DOPC) which is added to provide film fluidity, efficient packing, and optimal intermolecular contacts.[20] The binary nature of the lipid film makes it especially susceptible to interfacial shear, both in terms of its structure and its rheological response.[32]

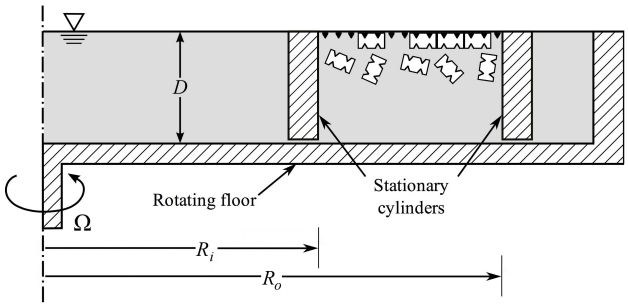


**Fig. 1** Schematic of the deep-channel surface viscometer flow geometry used for 2D protein crystallization. The protein (streptavidin) is shown as bow-ties and the ligand (biotin) is shown as triangles.

A number of experimental and computational techniques are utilized here, including surface velocimetry and numerical simulations of the flow at the interface coupled to the bulk flow, in order to understand the relationship between macro-scale forcing via shear in the vicinity of the interface and micro-scale response manifested as crystallization.

## 2 Experimental methods and materials

A schematic of the deep-channel surface viscometer used in this study is shown in Fig. 1. This flow has been extensively studied analytically, experimentally, and computationally.[33–38] The flow geometry consists of a liquid-filled annulus with stationary inner and outer cylinders of radii $R_i = 1.64$ cm and $R_o = 2.50$ cm, filled to the rim at a depth $D = 0.85$ cm, and a floor rotated at a constant rate, $\Omega$ rad/s. The cylinders were made of precision bore glass (Ace Glass, Trubore) and the floor was an optical window. The stationary cylinders are attached to a stainless steel bar which suspends them above the floor. The bar held the outer cylinder from the outside and held the inner cylinder from the inside, thereby avoiding any interference with the flow in the annular region. A larger cylinder was bonded to the floor to contain the liquid.

The geometry is characterized by the aspect ratio $A_1 = D/(R_o - R_i)$, and the radius ratio $A_2 = R_i/R_o$. For the experimental apparatus used in this study, these are $A_1 = 0.99$ and $A_2 = 0.656$. The flow strength is characterized by the Reynolds number,

$$Re = \rho \Omega R_o^2/\mu, \quad (1)$$

where $\rho$ (g/cm$^3$) is the density and $\mu$ (g/cm s) is the dynamic viscosity of the buffer. The interfacial hydrodynamics are also

governed by the Boussinesq number,

$$Bo = \mu^s / \mu R_o, \qquad (2)$$

where $\mu^s$ (g/s; surface Poise) is the surface (excess) shear viscosity, which is one of the two intrinsic interfacial viscosities in the Boussinesq–Scriven surface model.[39] The second interfacial viscosity, surface dilatational, does not play a dynamic role in the steadily-driven deep-channel flow. The four governing parameters are sometimes combined as $Re^* = Re(1-A_2)$ and $Bo^* = BoA_1/(1-A_2)$ to characterize the effects of inertia and surface viscosity. The surface films of interest exhibit large enough elasticity to inhibit any radial flow at the interface.[35] As reported in Azadani *et al.*[26], the zero radial interfacial flow provides an essentially uniform surface concentration.

The experiments reported here were conducted at 23°C with $\rho = 1.033$ g/cm$^3$ and $\mu = 9.95 \times 10^{-3}$ g/cm s which are about 3–4% higher than that of pure water. The crystals were imaged directly by a microscope (with a 10× objective and numerical aperture of 0.28) above the surface with a short pulse from an Nd:YAG laser (532 nm, 5 ns) transmitted up through the optical floor. The interfacial velocity profile was measured by tracking surface-bound protein clusters or crystals.[40] The experimentally measured velocity profiles were compared with computed velocity profiles that we obtained by solving the Navier–Stokes equations coupled to the Boussinesq–Scriven surface model, described in the following section.

The buffer solution was prepared with de-ionized water of resistivity greater than 18 MΩ cm and total organic carbon less than 5 ppb (Millipore, Simplicity 185-UV, fed with Poland Spring distilled water), by adding NaCl and $NaH_2PO_4$ to concentrations of 500 mM and 50 mM, respectively (Sigma Aldrich, catalog nos. 204439 and S0751, respectively). The pH of the buffer was measured to be $4.34 \pm 0.04$ using a pH meter (Fisher Scientific, Acument AB15). Finally, the buffer was filtered to remove any undissolved impurities (Millipore, 0.22 $\mu$m PES medium vacuum filter).

The lipid film consisted of a mixture of a biotinylated lipid and a diluting lipid. The biotinylated lipid was biotin-X-DHPE (lyophilized powder, Biotium, catalog no. 60023) and the diluting lipid was DOPC (dissolved in chloroform, Avanti Polar Lipids, catalog no. 850375C). Biotin-X-DHPE was dissolved in HPLC-grade chloroform and mixed with DOPC at a 1:10 mass-ratio (0.015 and 0.15 mg/ml, respectively). For experiments involving the deep-channel surface viscometer, a known concentration of the lipid film was spread on the air-water interface; the technique for spreading the film on the interface can be found in Azadani *et al.*[26] The isotherm, i.e. surface pressure Π [dyn/cm] as a function of area per molecule, A [Å$^2$/molecule], is shown in Fig. 2, where the present results are compared with Azadani *et al.*[26], showing good agreement. The surface tension measurement was obtained using a Wilhelmy plate during a slow compression (at least 15 minutes). In most of the experiments in the channel, Π was inferred from the Π–*A* isotherms, and verified by direct measurements for several experiments in the channel using the Wilhelmy plate. Π was measured before and after flow experiments and no measurable change in surface pressure was observed.

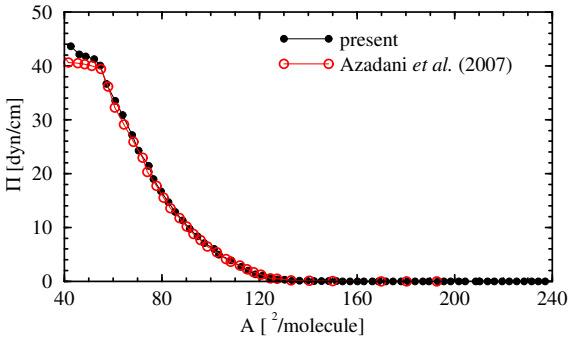


**Fig. 2** Equation of state, surface pressure Π [dyn/cm] versus area per molecule A [Å$^2$/molecule], for the binary lipid film (biotin-X-DHPE and DOPC) on the buffer at 23°C, measured in a Langmuir trough during a slow compression.

The protein streptavidin produced by the bacteria Streptomyces Avidinii was purchased (essentially salt-free lyophilized powder, Sigma-Aldrich, catalog no. S4762). The protein was dissolved in 50 mM $NaH_2PO_4$ (in DI water) at pH 8.2 at a concentration of 0.33 mg/ml. This pH was selected because it is far above the isoelectric point of the protein and it minimizes the turbidity of the solution. The solution was subsequently filtered using a 100 kDA regenerated cellulose filter (Millipore, catalog no. PLHK02510) and a 0.02 $\mu$m syringe filter (Whatman, catalog no. 6809-4012). We confirmed that the solution was free of detectable aggregates using a dynamic light scattering system (Wyatt, DynaPro Titan) both as a concentrated solution and after its injection in the buffer solution.

After spreading the binary lipid film, the protein solution was injected into the solution to a final concentration of 5 $\mu$g/ml. The solution was then kept quiescent for 60 minutes before flow was initiated by setting the floor to constant rotation. We waited about a viscous time (5 min) for the flow to reach steady state, and then used velocimetry to determine the interfacial velocity profile across the channel. The velocimetry took 30 to 60 minutes to complete. The interfacial velocity profile is used in conjunction with the numerical simulations to determine the surface shear viscosity. Once the velocimetry has been completed, the floor rotation is stopped. After about another 5 minutes, the flow comes to rest and the interface is sampled by lifting part of it with a piece of mica for subsequent imaging via high power microscopy.

## 3 Coupled interfacial and bulk hydrodynamics

### 3.1 Theoretical foundations

The flow in the deep-channel viscometer described in the previous section is governed by the Navier–Stokes equations with no-slip boundary conditions on the rotating floor and the stationary inner and outer cylinder walls, together with the tangential stress balance at the air-water interface. The system is non-dimensionalized using $R_o$ as the length scale and $1/\Omega$ as the time scale, and hence the velocity scale is $\Omega R_o$. The flow is assumed to remain axisymmetric. In cylindrical coordinates $(r,\theta,z)$, using the stream-function vorticity formulation, where the velocity is

$$\boldsymbol{u} = (u,v,w) = \left(-\frac{1}{r}\frac{\partial\psi}{\partial z}, v, \frac{1}{r}\frac{\partial\psi}{\partial r}\right), \tag{3}$$

and the vorticity is

$$\nabla\times\boldsymbol{u} = \left(-\frac{1}{r}\frac{\partial(rv)}{\partial z}, \eta, \frac{1}{r}\frac{\partial(rv)}{\partial r}\right), \tag{4}$$

where the azimuthal component of vorticity $\eta$ is

$$\eta = \frac{\partial u}{\partial z} - \frac{\partial w}{\partial r} = -\frac{1}{r}\left(\frac{\partial^2\psi}{\partial z^2} + \frac{\partial^2\psi}{\partial r^2} - \frac{1}{r}\frac{\partial\psi}{\partial r}\right), \tag{5}$$

the non-dimensional Navier–Stokes are

$$\frac{\partial v}{\partial t} + \frac{1}{r}\frac{\partial\psi}{\partial r}\frac{\partial v}{\partial z} - \frac{1}{r}\frac{\partial\psi}{\partial z}\frac{\partial v}{\partial r} - \frac{v}{r^2}\frac{\partial\psi}{\partial z} = \frac{1}{Re}\left(\frac{\partial^2 v}{\partial z^2} + \frac{\partial^2 v}{\partial r^2} + \frac{1}{r}\frac{\partial v}{\partial r} - \frac{v}{r^2}\right), \tag{6}$$

$$\frac{\partial\eta}{\partial t} - \frac{1}{r}\frac{\partial\psi}{\partial z}\frac{\partial\eta}{\partial r} + \frac{1}{r}\frac{\partial\psi}{\partial r}\frac{\partial\eta}{\partial z} + \frac{\eta}{r^2}\frac{\partial\psi}{\partial z} - \frac{2v}{r}\frac{\partial v}{\partial z} = \frac{1}{Re}\left(\frac{\partial^2\eta}{\partial z^2} + \frac{\partial^2\eta}{\partial r^2} + \frac{1}{r}\frac{\partial\eta}{\partial r} - \frac{\eta}{r^2}\right). \tag{7}$$

The no-slip boundary conditions on the stationary cylinder walls and the rotating floor are:

$$\text{Inner wall, } r = A_2: \qquad v = 0, \psi = 0, \eta = \frac{1}{A_2}\frac{\partial^2\psi}{\partial z^2}, \tag{8}$$

$$\text{Outer wall, } r = 1: \qquad v = 0, \psi = 0, \eta = \frac{\partial^2\psi}{\partial z^2}, \tag{9}$$

$$\text{Rotating floor, } z = 0: \qquad v = r, \psi = 0, \eta = \frac{1}{r}\frac{\partial\psi}{\partial r^2}. \tag{10}$$

The air-water interface is described using the Boussinesq–Scriven surface model,[34,36,39]. For a flat interface, only the tangential stress balance plays a dynamic role. We have previously demonstrated through experiments and computations[35,41,42] that at steady state, only a minuscule amount of surface elasticity is required in order for the surface tension gradient to eliminate any radial component of surface velocity. This is due to the small capillary number in the deep-channel viscometer. Furthermore, for the range of surface pressure considered here, the variation in the surface concentration of the film is negligible, and therefore the surface pressure is essentially uniform. Under such conditions, the radial stress balance at the interface is

$$\eta = -\frac{1}{r}\frac{\partial^2\psi}{\partial z^2}, \tag{11}$$

and the azimuthal tangential stress balance at the interface is

$$\frac{\partial v}{\partial z} = Bo\left(\frac{\partial^2 v}{\partial r^2} + \frac{1}{r}\frac{\partial v}{\partial r} - \frac{v}{r^2}\right). \tag{12}$$

The hydrodynamic system is governed by four parameters. Two describe the geometry, these are the depth-to-gap ratio, $A_1$ $(D/(R_o - R_i))$, and the radius ratio of the inner to outer cylinder, $A_2$ $(R_i/R_o)$. The Reynolds number, given in Eq. (1), is the ratio of a bulk viscous time scale, $\rho R_o^2/\mu$, to the time scale of the floor rotation, $1/\Omega$. The forth parameter is the Boussinesq number, given in Eq. (2), which gives the ratio of a bulk viscous time scale, $\rho R_o^2/\mu$, to a film viscous time scale, $\rho R_o^3/\mu^s$.

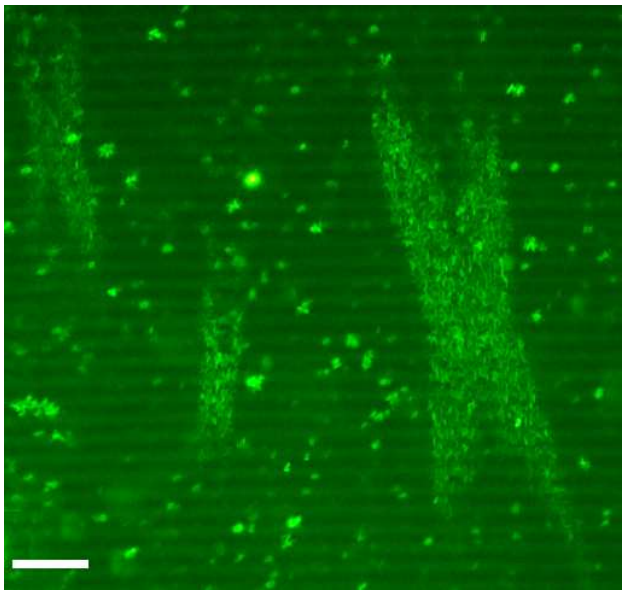

**Fig. 3** 2D crystals imaged directly at the interface, produced under quiescent conditions ($Re = 0$) at a surface pressure $\Pi = 10$ dyn/cm. The scale bar is 100 $\mu$m.

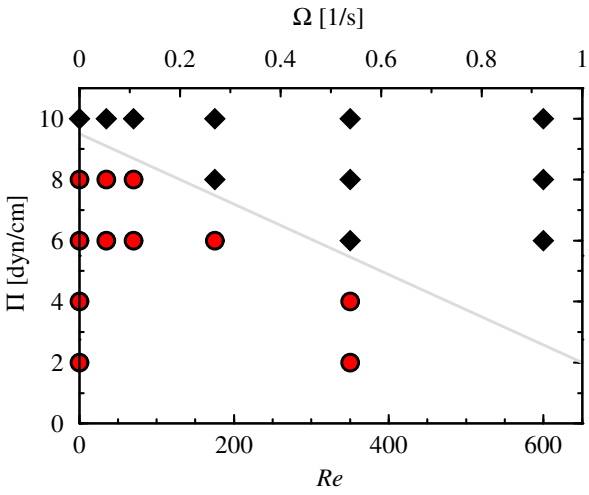


**Fig. 4** State diagram with surface pressure, Π [dyn/cm], and Reynolds number, *Re*, demarcating the parameter regimes where crystals form (diamonds) and do not form (circles); the gray line separating the two regimes is included to guide the eye.

### 3.2 Numerical implementation

The Navier–Stokes equations, Eqs. (5), (6), and (7) are solved in the bulk using a second-order centered finite-difference discretization in space and a second-order predictor-corrector (Heun's method) for time advancement. The method has been used and tested on internal rotating flows.[43] It has been extended to handle viscous and inviscid surface films.[35,41] The same implementation is used here, where Eqs. (11) and (12) are imposed at the interface. Knowing the interior bulk flow at any point in time, Eq. (11) is evaluated using second-order one-sided differences. As in other implementations,[35] Eq. (12) is solved for $v_s(r) = v(r, z = D/R_o)$ at each point in time with the just-computed interior solution $v(r,z)$ which is used to determine $v_z$ at the interface using second-order one-sided differences.

All of the results presented here have been computed with $n_r = n_z = 201$ grid points in the $r$ and $z$ directions. We have verified that doubling the grid resolution does not lead to appreciable differences in the solutions. The time step $\delta t$ used depends on *Re* (and the spatial resolution); for $Re < 10^2$ $\delta t \propto 1/Re$ and for $Re > 10^2$ we have kept $\delta t = 5 \times 10^{-3}$. Steady state is typically reached, when starting from rest, in about one viscous time based on depth ($\rho D^2/\mu$).

(a) Optical image

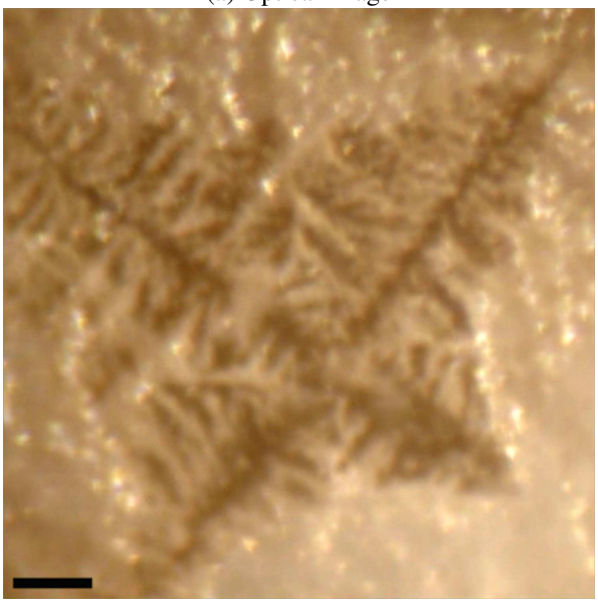

(b) TIRM image

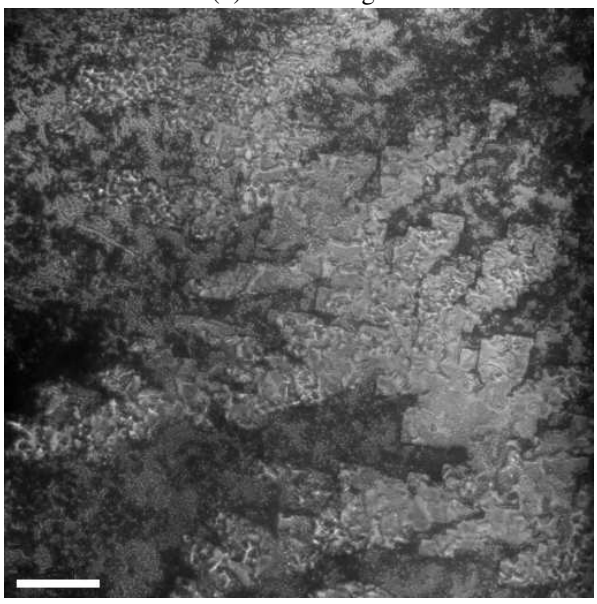

**Fig. 5** Flow-induced 2D protein crystals lifted off the interface for $Re = 350$ and $\Pi = 8$ dyn/cm; (a) shows an image using a conventional microscope with a 10× objective, and (b) shows another crystal imaged using TIRM. Scale bar in both images is 50 $\mu$m.

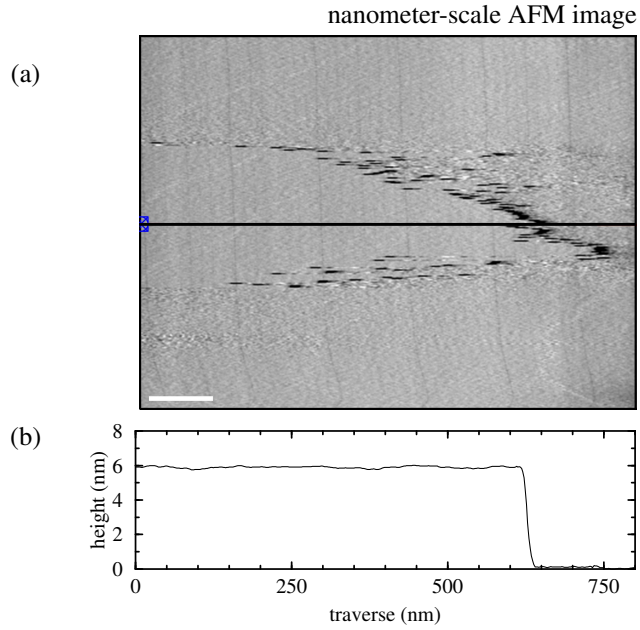


**Fig. 6** (a) AFM image (scale bar is 100 nm) of a flow-induced protein crystal lifted off the interface for $Re = 350$ and $\Pi = 8$ dyn/cm, together with (b) a graph of the height of the sample along the line in the AFM image.

## 4 Results

### 4.1 Quiescent 2D crystallization ($Re = 0$)

Under quiescent conditions, a variety of 2D crystal structures of streptavidin have been reported, depending primarily on the pH of the buffer solution.[13] Fig. 3 shows 2D H-shaped crystals of streptavidin that we have obtained under quiescent conditions ($Re = 0$) at a surface pressure $\Pi = 10$ dyn/cm, consistent with the surface pressure range at which Ratanabanangkoon[44] observed quiescent crystals. As well as the three prominent H-shaped crystals, there are film-bound protein clusters (appearing as bright dots) and aggregates visible in the field of view.

### 4.2 Flow-induced crystallization

Fig. 4 summarizes our experimental results, showing a delineation in surface pressure – Reynolds number ($\Pi$, $Re$) space between conditions where crystals are observed (diamonds) and are not observed (circles). Note that at $Re = 0$ (quiescent), the threshold for crystallization is $\Pi \gtrsim 10$, consistent with previous reports.[44] It is interesting that even though the flow geometry used in Azadani *et al.*[26] was different (a cylinder rather than an annulus), the threshold for crystallization that they observed for $Re = 1000$ was $\Pi \gtrsim 1$ dyn/cm, is consistent with an extrapolation of the threshold indicated in Fig. 4. For $Re \in [0, 600]$, Fig. 4 shows that the threshold for crystallization monotonically decreases with increasing $Re$.

The flow-induced crystals were found to be of dendritic X-shaped variety, in contrast to the H-shaped crystals obtained under quiescent conditions. Fig. 5(a) shows such a dendritic X-shaped crystal, induced by flow in the deep-channel surface viscometer at $Re = 350$ and $\Pi = 8$ dyn/cm, lifted off the interface and imaged using a conventional optical microscope, and Fig. 5(b) shows another crystal imaged using total internal reflection microscopy (TIRM). In order to obtain finer resolution measurements, such a crystal was also analyzed using atomic force microscopy (AFM). Fig. 6(a) shows an AFM height contour and Fig. 6(b) shows a cross-sectional profile measured along the horizontal line in Fig. 6(a). This confirms that the flow-induced crystal is of height 6 nm, as expected for a 2D streptavidin crystal ($5.9 \pm 0.5$ nm).[45]

### 4.3 Flow conditions associated with 2D crystallization

We begin by describing the bulk flows that drive the shearing interfacial flows computed from the model described in § 3.1. Fig. 7 shows vortex lines ($rv$) and streamlines ($\psi$) of typical steady states in the linear ($Re = 70$) and nonlinear ($Re = 600$) flow regimes for a few Boussinesq numbers $Bo$, illustrating the features of these steady states. It should be noted that these steady laminar axisymmetric states are stable to general 3D perturbations for $Re \lesssim 10^4$.[42] The primary flow is characterized by the vortex lines which emanate from the rotating floor. The vortex lines correspond to contours (isolines) of $rv$. These cannot terminate at the stationary cylinder walls nor in the interior of the flow, so they either terminate at the corners where the rotating floor meets the stationary cylinder walls, or at the interface. The angle at which the vortex lines meet the interface is dependent on the Boussinesq number $Bo$, as described by the tangential interfacial stress balance in Eq. (12). The bending of the vortex lines, either to satisfy no-slip boundary conditions at the solid boundaries or to satisfy the interfacial tangential stress balance, leads to the production of a secondary meridional flow via the $\frac{2v}{r}\frac{\partial v}{\partial z}$ term in Eq. (7), which is a source of azimuthal vorticity, $\eta$. The azimuthal vorticity, via Eq. (5), drives the secondary meridional flow which is characterized by the streamlines $\psi$. When the Reynolds number is small ($Re \lesssim 10^2$ for the flow geometry considered here), the flow is in the Stokes regime in which the redistribution of $rv$ produced at the rotating floor throughout the whole domain is dominated by molecular diffusion and the process is effectively decoupled from the secondary meridional flow; this is a linear flow regime. For higher $Re$, the strength of the secondary meridional flow is stronger, the redistribution of $rv$ is not decoupled from the meridional flow, and in fact the meridional flow plays an important role in its redistribution.

In what follows, we describe the interfacial shearing flow

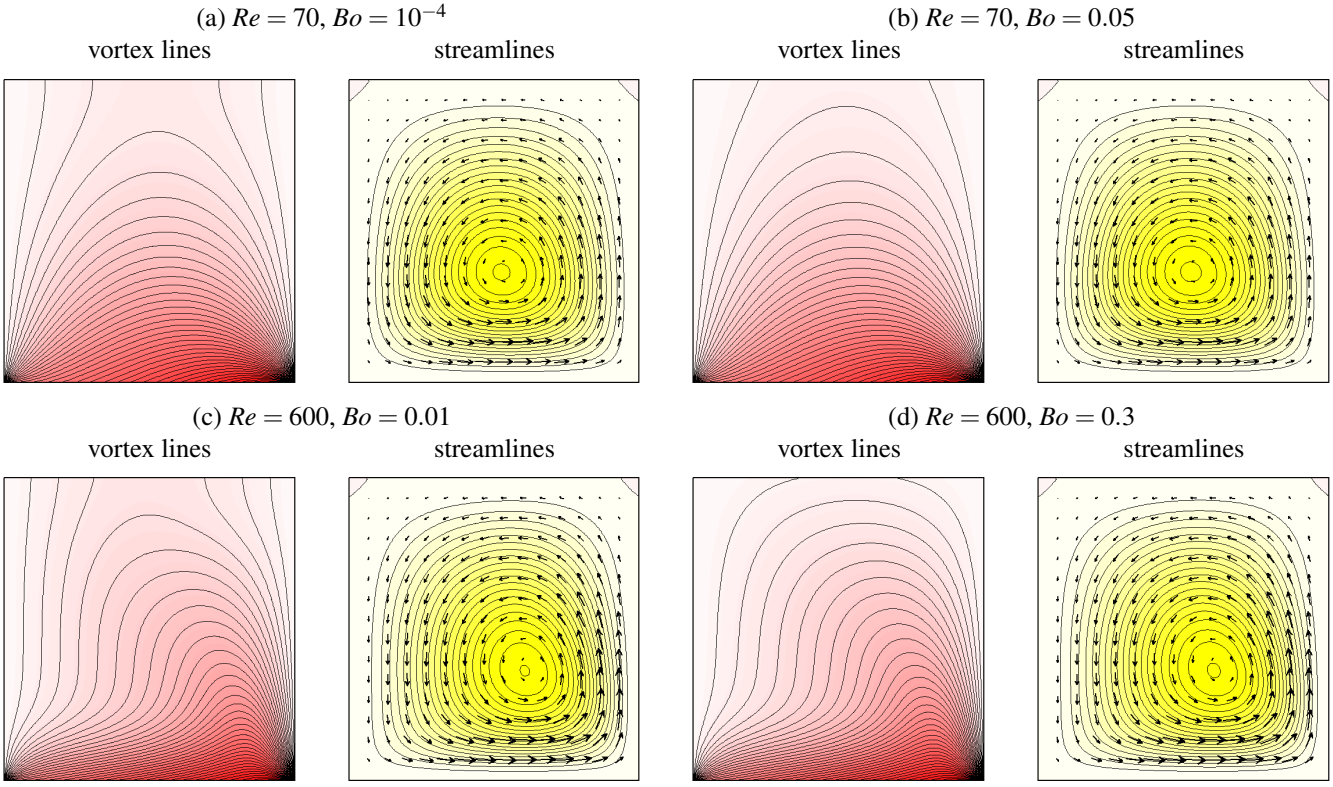


**Fig. 7** Vortex lines (contours of $rv$) and streamlines (contours of $\psi$) in the meridional plane $A_2 \le r \le 1$ and $0 \le z \le D/R_o$, at steady state for $Re$ and $Bo$ as indicated. There are 40 contours with $rv \in [0,1]$, and 20 contours with $\psi \in [-1.5\times10^{-3}, 0]$ for $Re = 70$ and $\psi \in [-7\times10^{-3}, 0]$ for $Re = 600$; the arrows indicate the meridional velocity $(u,w)$, they are tangential to the streamlines and their magnitude is proportional to the gradient in $\psi$ normal to the stream direction.

corresponding to the steady laminar flows at the various $Re$ and $Bo$. Fig. 8 presents the azimuthal velocity profile at the interface $v_s(r)$ at steady state; this is the only non-zero component of velocity at the interface. For $Re = 70$, which is in the linear flow regime, the profiles are essentially symmetric about the radial half-gap $(1-A_2)/2$, and their magnitude diminishes nonlinearly with increasing $Bo$ (in the limit $Bo \to \infty$, $v_s \to 0$; this follow directly from Eq. (12) with $Bo = \infty$ and boundary conditions at the stationary cylinder walls $v_s(r = A_2) = v_s(r = 1) = 0$). In the nonlinear regime ($Re = 600$), the profiles are not symmetric due to the meridional bulk flow advecting the vortex lines radially inward near the interface. The interfacial shear flow, $v_s$, is stronger (about 50% stronger in non-dimensional terms), as less $rv$ is lost to viscous dissipation at the higher $Re$.

In order to determine the surface shear viscosity of a given surface film experimentally, one measures the interfacial velocity at a given $Re$ and matches it to the interfacial velocity computed as described above for the same $Re$ and various $Bo$; the computed velocity profile that matches with the experimentally measured profile gives the $Bo$ of the film.

In order to investigate the flow conditions leading to crystallization, we measured the interfacial velocity field. The measurements confirmed that the radial component is negligible (on the order of experimental noise) and the only non-zero component of the velocity is in the azimuthal direction, denoted by $v_s(r)$, which has been non-dimensionalized by $\Omega R_o$. Fig. 9 shows $v_s(r)$ at two different floor rotation rates, corresponding to $Re = 70$ and 600. The symbols in the figure correspond to the measured profiles when the surface is covered by the binary lipid film at $\Pi = 8$ dyn/cm with protein injected in the buffer solution. The curves are computed profiles at those $Re$ for selected values of $Bo$ that bracket the experimental measurements of $v_s(r)$. Fig. 9(a) corresponds to $Re = 70$ at which no crystallization has occurred. In the $Re = 600$ case shown in Fig. 9(b), crystallization has occurred.

Fig. 9 reveals several important features of the interfacial flow field. The good agreement between the computed and measured velocity profiles show that at any given $Re$ the flow is Newtonian, albeit with different values of $Bo$. The shape

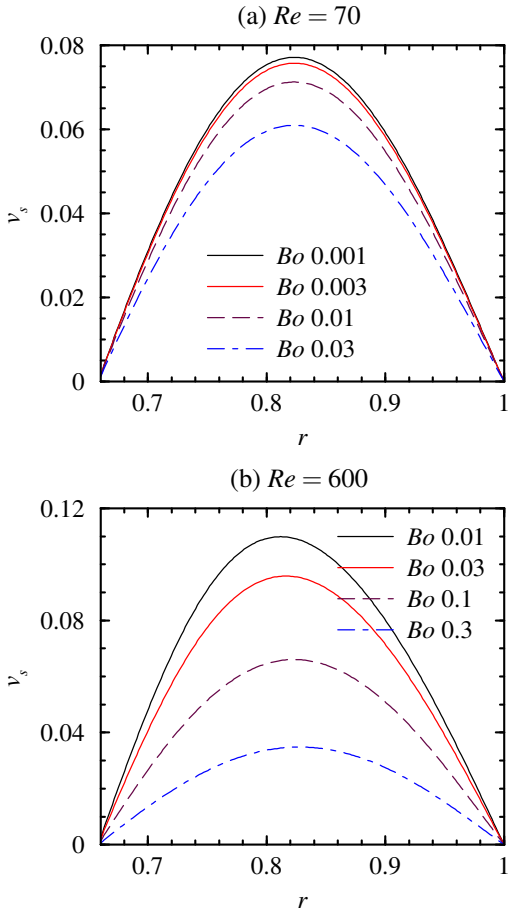


**Fig. 8** Radial profiles of computed non-dimensional surface azimuthal velocity $v_s$ (curves) across the annular gap, $r \in [A_2, 1]$, at various $Bo$ and $Re$ as indicated.

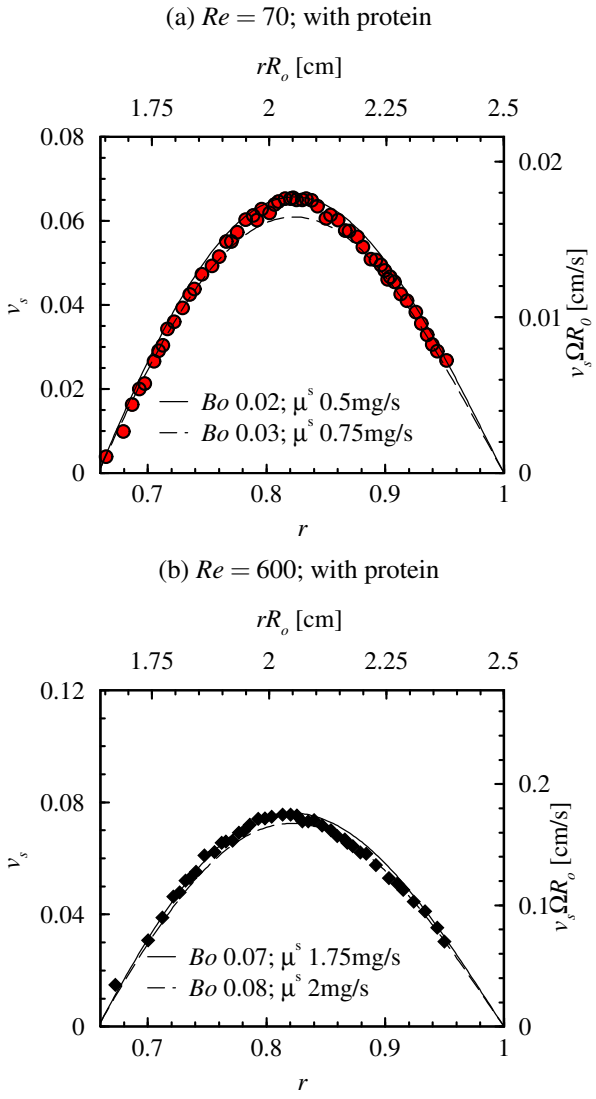


**Fig. 9** Radial profiles of computed non-dimensional surface azimuthal velocity $v_s$ (curves) across the annular gap, $r \in [A_2, 1]$, at various $Bo$ as indicated and experimentally measured $v_s$ on interfaces with protein at $\Pi = 8$ dyn/cm (symbols), and $Re$ as indicated. In the $Re = 70$ experiment (circles), the protein did not crystallize, and in the $Re = 600$ experiment (diamonds) the protein did crystallize.

of the measured velocity profile across the channel fits very well with the velocity computed with a Newtonian surface model, indicating that the flow of the film is Newtonian. This is not always the case, even for very strong flows with large Reynolds number. For example in Lopez *et al.* [46], in an experiment also conducted in a deep-channel surface viscometer, it was shown that monolayers of hemicyanine exhibit a velocity profile that is very similar to Newtonian predictions when the monolayer is at a low concentration but have a qualitatively different shape when the monolayer is at large concentrations. The flattened velocity profile obtained with such monolayers indicate that under those conditions the monolayer flow was not Newtonian.

Fig. 9 also shows that the non-dimensionalized velocity in the $Re = 600$ case is about 10% larger than for $Re = 70$, and the maximum in $v_s$ has shifted slightly (about 5% of the gap) inwards from the center. This is due to the nonlinearity associated with the flow inertia at large $Re$.[35] The dimensional data shown on the scale on the right of the figures emphasize how the local shear rate at the interface (essentially the radial gradient in dimensional surface azimuthal velocity) scales with $\Omega$ rad/s (and hence with $Re$); the plots show how the shear increases by about an order of magnitude when $\Omega$ ($Re$) is increased by the same amount. Finally, for $Re = 600$, where crystallization is observed, Fig. 9(b) shows that the $Bo$ is larger. Although it would be tempting to attribute the increase in $Bo$ as purely due to crystals, this may not be the case. The percentage of the interface covered by crystals is small, so it is unclear if they interact with each other and influence the surface shear viscosity. In order to begin to understand this increase in $Bo$ and the flow-induced crystallization in general, it is beneficial to decouple the effect of flow on binary lipid film from the effect of flow on both the film and protein. In the following subsection, we investigate the complicated response to flow of the binary phospholipid film without any protein.

### 4.4 Phospholipid film behavior in the absence of protein

Measurements of the azimuthal velocity profile at the interface, $v_s$, were repeated on the binary lipid film without any added protein. Fig. 10 shows the interfacial velocity profiles for the same two $Re$ as before (70 and 600) along with a pair of computed profiles for values of $Bo$ bracketing the measurements. In the absence of protein, Fig. 10 shows that although a single value of surface shear viscosity fits the measured velocity profile at a given Reynolds number, the surface shear viscosity does vary with $Re$.

Comparing the $v_s$ profiles withouth protein (Fig. 10) with those of Fig. 9, which had protein, we see that at a given $Re$, the presence of protein results in a more viscous interfacial film (larger $Bo$). We also have the same qualitative increase in $Bo$ with increasing $Re$. The important point here is that

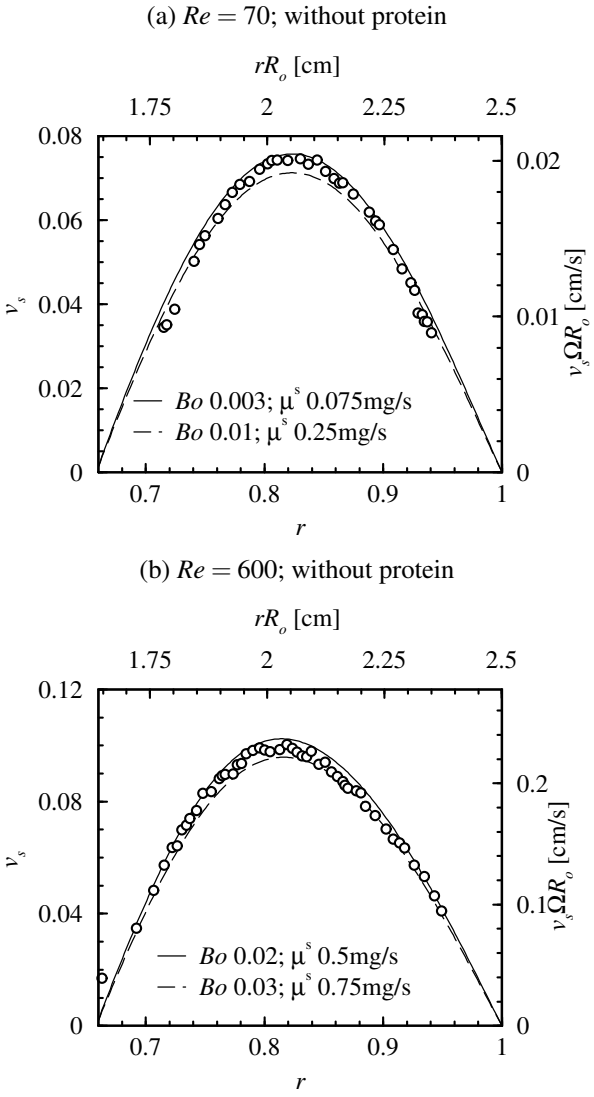


**Fig. 10** Radial profiles of computed non-dimensional surface azimuthal velocity $v_s$ (curves) across the annular gap, $r \in [A_2, 1]$, at various $Bo$ as indicated and experimentally measured $v_s$ on interfaces without protein at $\Pi = 8$ dyn/cm (symbols), and $Re$ as indicated.

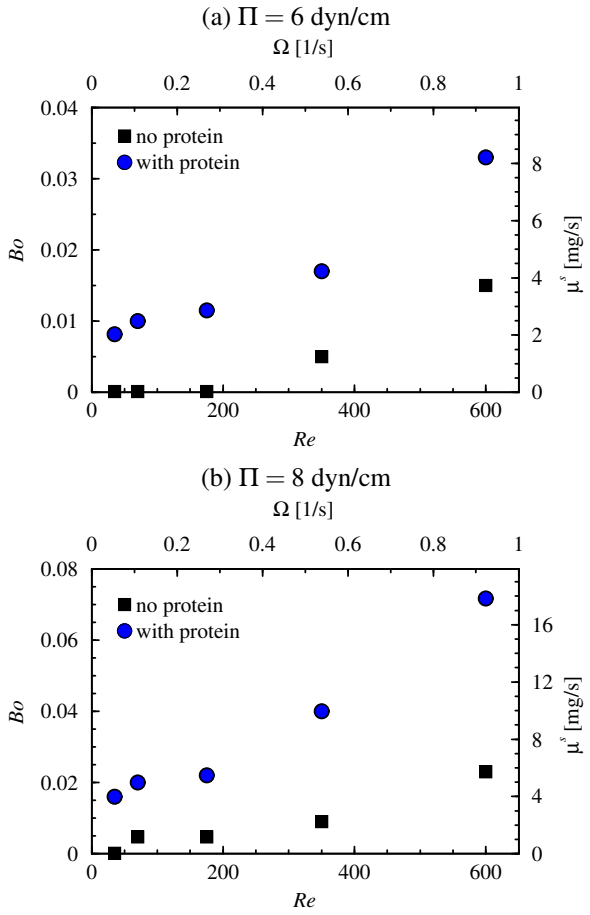


**Fig. 11** Surface shear viscosity, *Bo*, of an interface with compared to one without protein, as a function of *Re* for Π as indicated. The data using circles correspond to cases where the protein did not crystallize, and the data using diamonds correspond to cases where the protein did crystallize.

this increase is happening in the absence of protein, indicative of the complicated response of the binary lipid film to strong shear in the vicinity of the interface. This is not surprising given the rich rheological behavior of such lipid films.[32]

At larger $Re = 600$, the binary lipid film without protein exhibits a significantly larger non-dimensional velocity, commensurate with the effects of bulk flow inertia on interfacial velocity.[35] When protein is present, however, the velocity is drastically reduced and there is a corresponding increase in surface shear viscosity, $\mu^s$ (*Bo*).

Experiments with and without protein, similar to those presented in Figs. 9 and 10, were performed for additional *Re* and Π, and the surface shear viscosities, both in dimensional and non-dimensional form, are presented in Fig. 11. For every case, Fig. 11 shows that the surface shear viscosity is al-

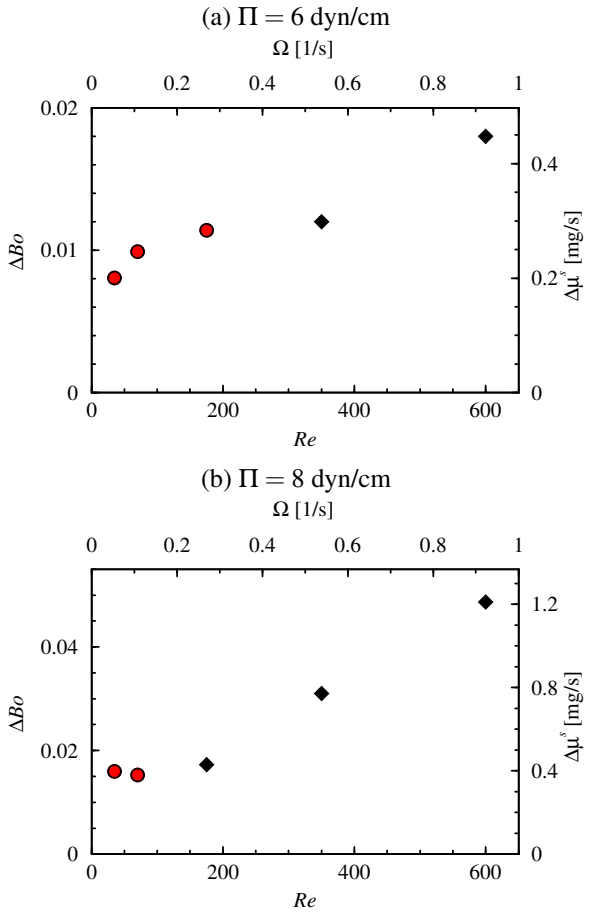


**Fig. 12** Increase in the surface shear viscosity, Δ*Bo*, of an interface with compared to one without protein, as a function of *Re* for Π as indicated. The data using circles correspond to cases where the protein did not crystallize, and the data using diamonds correspond to cases where the protein did crystallize.

ways larger when protein is present. As expected, the surface shear viscosity is not independent of Π, nor is it independent of *Re*. Fig. 12 presents the results in terms of Δ*Bo*, the increase in surface shear viscosity due to the presence of protein at the same Π and *Re*. Δ*Bo* is always found to be positive, and upon inception of flow-induced crystallization, Δ*Bo* increases rapidly with *Re*. The experiments were repeated several times to ensure reproducibility of the results. The increase in *Bo* is apparently due to interactions between protein-ligand complexes. The same qualitiative increase in Δ*Bo* occurs upon crystallization for both surface pressures.

## 5 Discussion and conclusions

We have shown that over a wide range of conditions, shearing flows can induce 2D protein crystallization at an air-water interface with a ligand-bearing binary lipid film. The 2D protein crystals induced by flow were of a different morphology than those grown quiescently. The strength of the flow is characterized by the Reynolds number, *Re*, as is the shear in the vicinity of the interface. Experiments demonstrate that with stronger flow, smaller surface pressure is needed to form crystals.

Streptavidin is tetrameric with four biotin binding sites, two on the side of the molecule that bind to the biotinylated monolayer, and two that face the bulk solution. The crystal lattice unit cell area for a 2D streptavidin crystal has been shown to be 2900–6700 Å$^2$, depending on crystal morphology,[12] which is of the same order as the spacing between the biotin molecules prior to injection of the protein (1260–1680 Å$^2$/molecule). Therefore, it can be concluded that the liquid-phase protein-laden interface is unstable (or supersaturated) and susceptible to crystallize. This also suggests that when sufficient amount of protein is injected into the bulk to bind to all of the biotin molecules at the interface (at least 0.5 $\mu$g/ml in the present geometry), the packing density of the protein at the interface is determined by the concentration of the ligand-bearing lipid at the interface, and not the concentration of protein in the bulk. Thus, the surface pressure, Π, representing the packing density of the lipid layer, gives a qualitative measure of the supersaturation.

Shear in the vicinity of the interface appears to be responsible for flow-induced crystallization, the shear in the vicinity of the interface alters the protein-ligand complexes. It is likely that shear affects the nucleation rather than the crystal growth since crystals were induced by flow at conditions where crystals are never observed under quiescent conditions. Shear has also been identified as the mechanism behind flow-induced crystallization of other macromolecules, namely, polymer melts.[47–49] Kobayashi and Nagasawa[50] postulated that flow-induced polymer crystallization takes place because of a decrease in the entropy difference between the crystalline and liquid states due to the presence of shear, thus lowering the free energy barrier between the liquid and crystal state,[51] and promoting nucleation and ultimately crystal growth.

It has long been established that the fluidity of the interfacial film is essential for 2D protein crystallization.[20] In the absence of bulk flow, diffusive processes control motion of the protein-ligand complexes at the interface. Shearing the interface is seen to enhance 2D protein crystallization. The question then arises as to how it works. It has been theorized that nucleation of protein crystals occurs in two steps: formation of a cluster of a dense liquid, metastable with respect to the crystalline state, followed by ordering within this cluster to produce a crystal.[52] It is possible that shear, through its inherent anisotropy, aids in the ordering of the dense liquid precursors of nucleation,[26] thus lowering the entropy of the liquid state. At sufficiently high levels of shear, the free energy barrier vanishes and the system proceeds to the crystalline state.

The degree of supersaturation is quantified by the surface pressure, Π. For a given Π, the surface shear viscosity of the binary phospholipid mixture was found to be strongly dependent on *Re*. This is not necessarily a non-Newtonian effect. The rationale for this conclusion is that at any given *Re*, the coupled Newtonian interfacial and bulk hydrodynamic model reproduces the measured interfacial velocity profiles for appropriate values of the surface shear viscosity.

The measured Reynolds number-dependent response of the binary phospholipid mixture is consistent with the complex behavior observed by others in a variety of lipid films.[53–56] Espinosa *et al.*[32], who also utilized a macroscale surface shear viscometer, reported fundamental differences between the response of saturated and unsaturated lipids and their mixtures. Given that the two lipids comprising the binary mixture in our study have different degrees of saturation (biotin-X-DHPE is di-saturated and DOPC is di-unsaturated), it is plausible that the complex response extends beyond measurements of surface shear viscosity, and that their interaction with flow is responsible for this *Re* dependence. Recently, Sadoughi *et al.*[57] found that in another phospholipid, the lung surfactant component DPPC, its response to flow and interfacial shear is linear over a wide range of surface pressures, and a single value of surface shear viscosity fits the measurements of the velocity profile across a deep-channel surface viscometer. In their study, the surface shear viscosity for DPPC was also shown to be *Re* dependent.

Finally, it should be noted that shear in the vicinity of the interface may alter the structure of the ligand-bearing binary film, thereby inducing protein crystallization. That would explain the complex response to shear by the binary lipid film in the absence of protein. Further study of the binary film in the absence of protein is warranted as it may shed more light on the mechanism for flow-induced protein crystallization.

## Acknowledgments

This work was supported by the National Science Foundation grants CBET-1064644 and CBET-1064498, and NASA grant NNX13AQ22G. We would also like to thank Aditya Raghunandan and Christopher F. Tilger for their assistance with some of the experiments using BAM.

## References

1 H.-S. Cho, K. Mason, K. X. Ramyar, A. M. Stanley, S. B. Gabelli, D. W. Denney and D. J. Leahy, *Nature*, 2003, **421**, 756–760.
2 T. Zhou, I. Georgiev, X. Wu, Z.-Y. Yang, K. Dai, A. Finzi, Y. D. Kwon, J. F. Scheld, W. Shi, L. Xu, Y. Yang, J. Zhu, M. C. Nussenzweig, J. Sodroski, L. Sharpiro, G. J. Nabel, J. R. Mascola and P. D. Kwong, *Science*, 2010, **13**, 811–817.
3 Y. Koldobskaya, E. M. Duguid, D. M. Shechner, N. B. Suslov, J.-D. Ye, S. S. Sidhu, D. P. Bartel, S. Koide, A. A. Kossiakoff and J. A. Piccirilli, *Nature Struct. Molec. Biol.*, 2011, **18**, 100–106.
4 A. McPherson, *J. Struc. Biol.*, 2003, **142**, 1–2.
5 M. Riès-Kautt, I. Broutin, A. Ducruix, W. Shepard, R. Kahn, N. Chayen, D. Blow, K. Paal, W. Littke, B. Lorber, A. Thòbald-Dietrich and R. Giege, *J. Cryst. Growth*, 1997, **181**, 79–96.
6 L. Chaiet and F. J. Wolf, *Arch. Biochem. Biophys.*, 1964, **106**, 1–5.
7 N. M. Green, *Methods Enzymol.*, 1990, **184**, 51–67.
8 E. A. Bayer, H. Ben-Hur and M. Wilcheck, *Methods Enzymol.*, 1990, **184**, 217–233.
9 A. A. Darst, M. Ahlers, P. H. Meller, E. W. Kubalek, R. Blankenburg, H. O. Ribi, H. Ringsdorf and R. D. Kornberg, *Biophys. J.*, 1991, **59**, 387–396.
10 S. A. Hemming, A. Bochkarev, S. A. Darst, R. D. Kornberg, P. Ala, D. S. C. Yang and A. M. Edwards, *J. Mol. Biol.*, 1995, **246**, 308–316.
11 W. Frey, W. R. Schief and V. Vogel, *Langmuir*, 1996, **12**, 1312–1320.
12 S.-W. Wang, C. R. Robertson and A. P. Gast, *J. Phys. Chem. B.*, 1999, **103**, 7751–7761.
13 S.-W. Wang, C. H. Robertson and A. P. Gast, *Langmuir*, 1999, **15**, 1541–1548.
14 T. C. Edwards, N. Malmastadt, S. Koppenol, H. Masahiko, V. Vogel and P. S. Stayton, *Langmuir*, 2002, **18**, 7447–7451.
15 P. Ratanabanangkoon and A. P. Gast, *Langmuir*, 2003, **19**, 1794–1801.
16 C. E. Chivers, E. Crozat, C. Chu, V. T. Moy, D. J. Sherratt and M. Howarth, *Nat. Methods*, 2010, **7**, 391–393.
17 T. Wang, R. Sha, R. Dreyfus, M. E. Leunissen, C. Maass, D. J. Pine and P. M. Chaikin, *Nature*, 2011, **478**, 225–229.
18 J. Zhao, J. Wu and S. L. Veatch, *Biophys. J.*, 2013, **104**, 825–834.
19 C. Phurimsak, E. Yildirim, M. D. Tarn, S. J. Trietsch, T. Hankemeier, N. Pamme and P. Vulto, *Lab Chip*, 2014, **14**, 2334–2343.
20 C. Vénien-Bryan, P.-F. Lenne, C. Zakri, A. Renault, A. Brisson, J.-F. Legrand and B. Berge, *Biophys. J.*, 1998, **74**, 2649–2657.
21 P.-F. Lenne, B. Berge, A. Renault, C. Zakri, C. Vénien-Bryan, S. Courty, F. Balavoine, W. Bergsma-Schutter, A. Brisson, G. Grbel, N. Boudet, O. Komovalov and J.-F. Legrand, *Biophys. J.*, 2000, **79**, 496–500.
22 L. Drazek, J.-F. Legrand and L. Davoust, *J. Crystal Growth*, 2005, **275**, 1467–1472.
23 *Proteins at Liquid Interfaces*, ed. D. Möbius and R. Miller, Elsevier, 1998.
24 J. Krägel, S. R. Derkatch and R. Miller, *Advances in Colloid and Interface Science*, 2008, **144**, 38–53.
25 D. B. Allan, D. M. Firester, V. P. Allard, D. H. Reich, K. J. Stebe and R. L. Leheny, *Soft Matter*, 2014, DOI: 10.1039/c4sm00484a.
26 A. N. Azadani, J. M. Lopez and A. H. Hirsa, *Langmuir*, 2007, **23**, 5227–5230.
27 D. Roehm, S. Kesselheim and A. Arnold, *Soft Matter*, 2014, DOI: 10.1039/c4sm00686k.
28 J. E. Young, *PhD thesis*, Rensselaer Polytechnic Institute, 2013.
29 S. Munro, *Cell*, 2003, **115**, 377–388.
30 S. L. Veatch and S. L. Keller, *Phys. Rev. Lett.*, 2005, **94**, 148101.
31 G. van Meer, D. R. Voelker and G. W. Feigenson, *Nat. Rev. Molec. Cell Biol.*, 2008, **9**, 112–124.
32 G. Espinosa, I. López-Montero, F. Monroy and D. Langevin, *Proc. Nat. Acad. Sci. USA*, 2011, **108**, 6008–6013.
33 R. J. Mannheimer and R. S. Schechter, *J. Colloid Interface Sci.*, 1970, **32**, 195–211.
34 D. A. Edwards, H. Brenner and D. T. Wasan, *Interfacial Transport Processes and Rheology*, Butterworth-Heinemann, Boston, 1991.
35 A. H. Hirsa, J. M. Lopez and R. Miraghaie, *J. Fluid Mech.*, 2002, **470**, 135–149.
36 J. C. Slattery, L. Sagis and E.-S. Oh, *Interfacial Transport Phenomena*, Springer: New York, 2nd edn, 2007.
37 S. R. Derkatch, J. Krägel and R. Miller, *Colloid J.*, 2009, **71**, 1–17.
38 R. Miller, J. K. Ferri, A. Javadi, J. Krägel, N. Mucic and R. Wüstneck, *Colloid Polym. Sci.*, 2010, **288**, 937–950.
39 L. E. Scriven, *Chem. Engng. Sci.*, 1960, **12**, 98–108.
40 A. N. Azadani, J. M. Lopez and A. H. Hirsa, *J. Colloid Interface Sci.*, 2008, **322**, 79–86.
41 J. M. Lopez and A. Hirsa, *J. Colloid Interface Sci.*, 2000, **229**, 575–583.
42 A. H. Hirsa, J. M. Lopez and R. Miraghaie, *J. Fluid Mech.*, 2001, **443**, 271–292.
43 J. M. Lopez, *J. Fluid Mech.*, 1990, **221**, 533–552.
44 P. Ratanabanangkoon, *PhD thesis*, Stanford University, 2002.
45 A. Schmidt, J. Spinke, T. Bayerl, E. Sackmann and W. Knoll, *Biophys. J.*, 2008, **63**, 1385.
46 J. M. Lopez, R. Miraghaie and A. H. Hirsa, *J. Colloid Interface Sci.*, 2002, **248**, 103–110.
47 R. H. Somani, B. S. Hsiao and A. Nogales, *Macromolecules*, 2001, **34**, 5902–5909.
48 S. Coppola, L. Balzano, E. Gioffredi, P. L. Maffettone and N. Grizzuti, *Polymer*, 2004, **45**, 3249–3256.
49 A. K. Doufas, A. J. McHugh and C. Miller, *J. Non-Newtonian Fluid Mech.*, 2000, **92**, 27–66.
50 K. Kobayashi and T. Nagasawa, *J. Macromol. Sci. – Phys.*, 1970, **B4**, 331–345.
51 D. Kashchiev, *Nucleation: Basic Theory with Applications*, Butterworth–Heinemann, Oxford, 2000.
52 P. G. Vekilov, *Crystal Growth & Design*, 2004, **4**, 671–685.
53 J. Krägel and S. R. Derkatch, *Current Opinion in Colloid & Interface Sci.*, 2010, **15**, 246–255.
54 B. S. Murray, *Current Opinion in Colloid & Interface Sci.*, 2011, **16**, 27–35.
55 A. R. Honerkamp-Smith, F. G. Woodhouse, V. Kantsler and R. E. Goldstein, *Phys. Rev. Lett.*, 2013, **111**, 038103.
56 T. T. Hormel, S. Q. Kurihara, M. K. Brennan, M. C. Wozniak and R. Parthasarathy, *Phys. Rev. Lett.*, 2014, **112**, 188101.
57 A. H. Sadoughi, J. M. Lopez and A. H. Hirsa, *Phys. Fluids*, 2013, **25**, 032107.

Predictive modeling of biofilm flows, based on first principles, is used to quantify 2D protein crystallization on a ligand-bearing phospholipid film at the air-water interface.